SOFT ROBOTICS
Volume 00, Number 00, 2020

DOI: 10.1089/soro.2020.0001

SoRo
Soft Robotics

Soft Humanoid Hands with Large Grasping Force Enabled by Flexible Hybrid Pneumatic Actuators

Xiaomin Liu,[1,2] Yunwei Zhao,[1] Dexu Geng,[1] Shoue Chen,[2] Xiaobo Tan,[3] and Changyong Cao[2,3]

Abstract

Soft grippers and actuators have attracted increasing attention due to safer and more adaptable human–machine and environment–machine interactions than their rigid counterparts. In this study we present a novel soft humanoid hand that is capable of robustly grasping a variety of objects with different weights, sizes, shapes, textures, and stiffnesses. The soft hand fingers are made of flexible hybrid pneumatic actuators (FHPAs) designed based on a modular approach. A theoretical model is proposed to evaluate the bending deformation, grasping force, and loading capacity of the FHPAs, and the effects of various design parameters on the performance of the FHPA are investigated for optimizing the soft hands. This new FHPA achieves a balance of required flexibility and necessary stiffness, and the resulting soft humanoid hand has the merits of fast response, large grasping force, low cost, light weight, and ease of fabrication and repair, which shows promise for a variety of applications such as fruit picking, product packaging, and manipulation of fragile objects.

Keywords: soft humanoid hand, soft pneumatic actuator, flexible hybrid pneumatic actuators, rigid-flexible coupling, soft robotics

Introduction

End effectors or grippers are an essential component of a robot as they facilitate the contact with a manipulated object, ensuring its position and orientation while a specific task is being performed.[1,2] Design of a gripper system requires considering important factors such as the developed force, stiffness/compliance, dexterity, and number of degrees of freedom (DOFs).

Traditional rigid grippers for industrial applications are generally made of simple but reliable rigid structures that help in generating large forces, high accuracy, and repeatability.[3] The large force applied by such a rigid gripper, however, can deform or even damage the manipulated objects. In addition, the hard structure and potentially large mass and associated inertia of a rigid gripper could cause severe injuries in possible collisions between humans and robots. Thus, to enable safer human–machine and environment–machine interactions,[4–6] the applications of soft grippers made from components of low stiffness have attracted increasing attention for an inherently safe and adaptive contact with humans and environments.[7–9]

Soft grippers are attractive because they not only can easily adapt to objects of various forms and weights but also achieve a conformal contact without the need for sophisticated control.[5,10–12] Soft grippers have been explored for a variety of applications, such as grasping irregular and/or fragile objects,[13–15] noninvasive surgical procedures,[16] wearable and field robotics,[17,18] and assistive devices or prosthetic artificial organs[19] among others. The actuation modes of soft grippers can be classified into three major categories: pneumatic[20,21] or hydraulic pressure driven,[22] tendon or cable driven,[23,24] as well as soft active material driven (e.g., shape memory alloy, electroactive polymer).[24–27] Among these, soft pneumatic grippers have demonstrated particular promise in achieving compliant grasping, simple but accurate control, low cost, robust actuation, and ease in fabrication.[28]

For example, Shapiro *et al.*, inspired by bimetallic strips, put forward a pneumatic bending actuator made of two materials with different shear moduli.[29] Mosadegh *et al.* described actuators based on Pneu-Nets, which generally consisted of an extensible top layer and an inextensible but flexible bottom layer.[13] Giannaccini *et al.* proposed a soft

[1]School of Mechanical Engineering, Beihua University, Jilin, Jilin, China.
[2]Laboratory for Soft Machines and Electronics, School of Packaging, Michigan State University, East Lansing, Michigan, USA.
[3]Departments of Mechanical Engineering, Electrical and Computer Engineering, Michigan State University, East Lansing, Michigan, USA.

gripper that used tendons to deform and flex a fluid-filled soft deformable container.[30] Galloway *et al.* designed a soft gripper that utilized hydraulic pressure for subsea applications.[31] Homberg *et al.* developed soft continuum fingers consisting of an expanding pneumatic layer bonded to a nonextensible flexible layer.[32] Recently, direct three-dimensional (3D) printing of soft pneumatic actuators was also presented using the fused deposition modeling technology.[21] Reviewing the designs of pneumatically driven soft actuators, one realizes that although completely soft pneumatic actuators can make full use of the features of soft materials, they also demonstrate some inherit disadvantages, such as being easily broken when contacting sharp surfaces, poor stability in grasping unbalanced loads, relatively weak grasping force for handling heavy loads, as well as large volume of air needed for actuation of an expanded bladder.

To augment the performance of soft robots, hybrid actuators that combine both rigid components and soft structures have been proposed to control their actuation characteristics. For instance, Chen *et al.* designed a hybrid bending actuator inspired by crustaceans, wrapping a hard exoskeleton on surface of soft actuators.[33] They demonstrated a bending angle of 230° under 120 kPa and the output force of 4 N at 165 kPa. Inspired by the morphology of arachnids, Nemiroski *et al.* utilized thin, lightweight, and rigid links actuated by inflatable balloon joints in combination with antagonistic tendons to achieve passive retraction.[34] The joint from this work could generate a force of 1200 mN when air pressure of 200 kPa was applied. However, the slow actuation speed of the joint and the limited mechanical properties of materials significantly constrained its broad applications. Fu *et al.* proposed a spring-reinforced actuator (SRA) by integrating a closed-coil spring into a central lumen of a three-chamber soft actuator.[35] They utilized the common mold-casting approach for building the soft body of SRA with silicone materials, leading to a complicated fabrication process.

In this work, we propose a new design of soft humanoid hand capable of robustly grasping a variety of objects with different weights, sizes, shapes, textures, and stiffnesses. The fingers of the soft hand are made of flexible hybrid pneumatic actuators (FHPAs) based on a modular approach. The FHPA consists of four major components: inner elastic bladder, outer rigid constraining rings, elastic skeleton, and end covers, which are all independent and assembled together using mechanical connections. A theoretical model is proposed to analyze the deformation of the soft finger actuator and further to predict the grasping force and the loading capacity of the assembled hand. In addition, the effect of design parameters on the performance of the FHPAs is investigated in detail for optimizing the soft hands. This new soft humanoid hand has the merits of fast response, large grasping force, low cost, lightweight, and ease of fabrication, installation, and repair.

Materials and Methods

Materials and fabrication of FHPA

All the constraining rings and end covers are 3D printed with ABS plastics. A rubber tube (Dalian Latex) is first trimmed to a desired length and then sealed on its ends with aluminum alloy plugs. The bottom plug is screw threaded to connect with the end cover. To ensure the air tightness, the constraining rings are set in advance for actuation test. Then, a leaf spring (65Mn or Stainless steel) is fixed onto the end cover, which is provided with a matching installation groove to constrain the bending direction of the actuator. Both the upper and lower ends of the leaf spring and the end covers are provided with mounting holes, and the leaf spring is firmly connected to the end covers by a screw. This mechanical connection greatly reduces the difficulty of installation and also makes it possible to replace components. Next, a set of constraining rings are installed onto the rubber tube and the leaf spring. After that, the top-end cover is assembled with the leaf spring and a threaded plug. The bottom-end cover is finally connected with a pneumatic connector (SMC) for pump actuation.

Measuring bending deformation and angles of FHPA

An experimental setup is built to measure the bending deformation and bending angle of the FHPA under different conditions (Supplementary Fig. S1). The controller controls the pneumatic system in which the proportional valves (ITV0050-3BS) and solenoid valves (SMC-PSE560) adjust the pressure of the actuators. There are six markers pasted on the FHPA, and the motion trajectories of markers on FHPAs are captured by a 3D motion capture system (Optotrak). Then the change of lengths and curvature radius of actuators can be captured by the motion trajectory of markers. In addition, the bending angles of the FHPA are measured by gyroscope sensor (MPU-6050, InvenSense, Inc.) mounted at the front end of the actuator Supplementary Video S1.

Measuring FHPA actuation forces

The bottom end of the actuator is fixed, and the probe of the force sensor (Capacity 100 N) touches the measurement point (L is from 0 to 60 mm, in steps of 4 mm) at the initial state. Then, the applied air pressure is increased from 0 to 0.3 MPa with a step size of 0.1 MPa to actuate the FHPA; in this process the actuation force at the measuring point is recorded by the force sensor. The force sensor is mounted on the slide, and the measuring point can be adjusted by moving the force sensor with the slide. After the output force at one point is measured, the force sensor is then moved to the next position to measure again. A 6D force sensor is used to measure the normal force of the actuator. With a certain prebending angle of the actuator, the force sensor, which is installed on the cross slide, is adjusted to contact the actuator and then measure force under different air pressures.

Results and Discussion

Figure 1a presents the prototype of a soft humanoid hand made of five FHPAs, which has a weight of only 350 g and is about 1.5 times size of a typical human hand. The humanoid hand is designed to be symmetrical with four fingers evenly distributed at the front of a relatively rigid hand palm and one thumb located in the center of the palm (Fig. 1a). The humanoid hand has five DOFs, and the four fingers can actively bend toward the inside of the palm. Different from those four fingers, the thumb is positioned on the opposite side and tilted at a 75° angle with the palm and is equipped with two pneumatic chambers to enhance the clamping force in grasping operations. In addition, the fingertips and the

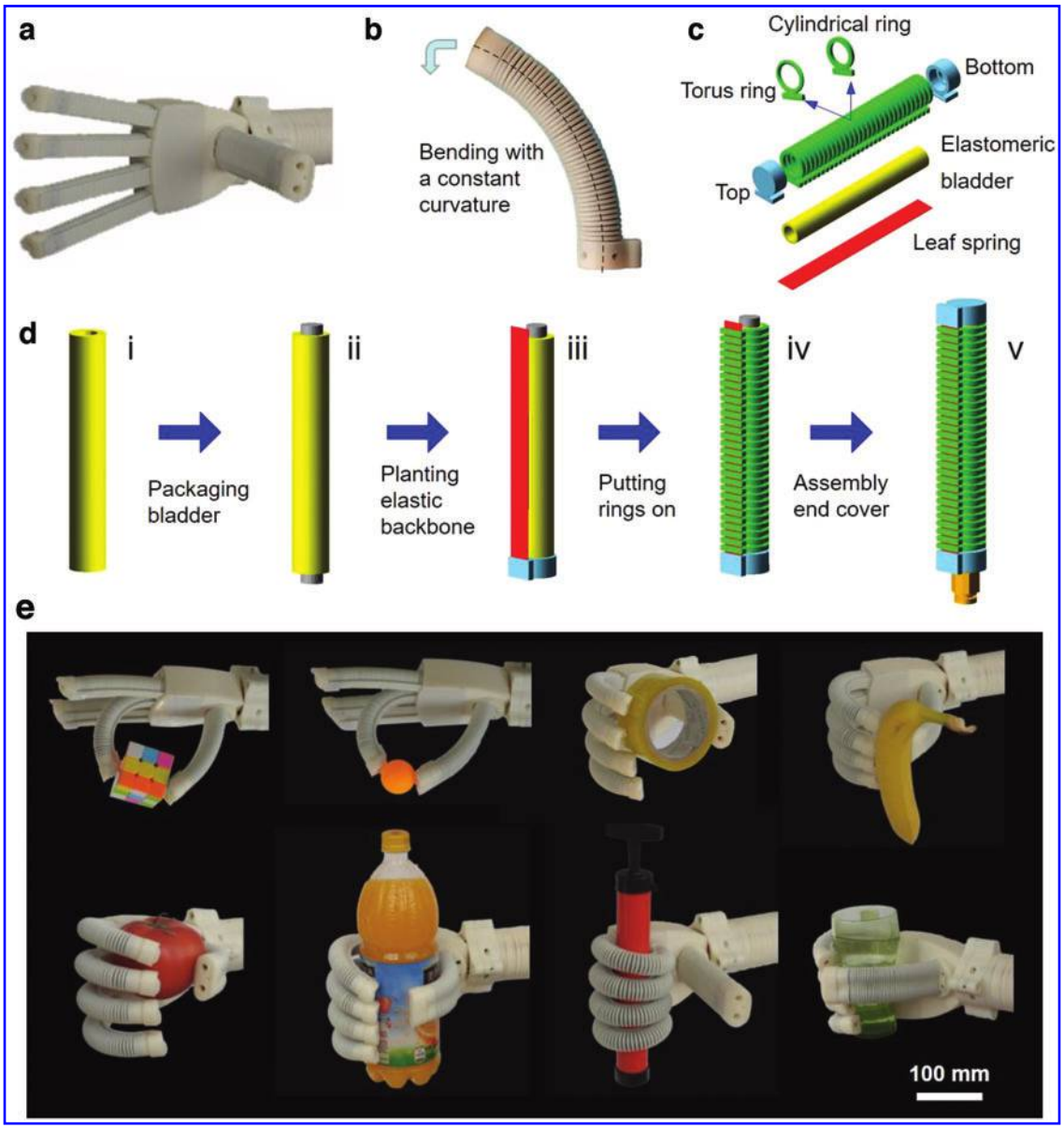

FIG. 1. The proposed FHPA and flexible humanoid hand. **(a)** Prototype of a humanoid gripper assembled with five FHPAs. **(b)** Bending deformation of a FHPA under air pressure actuation. **(c)** Schematic illustration of the components of a FHPA. **(d)** Schematic illustration of the fabrication process of a FHPA. **(e)** Demonstration of grasping a variety of objects by the fabricated soft humanoid hand: Rubik's cube (85 g), table tennis ball (3 g), cylinder (253 g), banana (232 g), tomato (329 g), bottled juice (1366 g), thin cylinder (98 g), and water glass (615 g). FHPA, flexible hybrid pneumatic actuator. Color images are available online.

silicone pads on the palm are patterned with textures to increase the friction.

The FHPA is mainly composed of an inner elastomeric bladder, a series of external constraint rings, a leaf spring as the elastic backbone, and two terminal covers (Fig. 1c). To achieve high elasticity and good stretching capacity of the gripper finger, commercially available latex or silicone tubes are used as inner elastomeric bladder with the deformation range of $\sim$200% to −500%.[36] A set of 3D-printed rigid rings are placed along the finger tube to restrict the radial expansion of the inner elastomeric bladder. The rings are independent and movable along the elastomeric bladder so that they can rotate freely around the bladder tube during bending actuation by air pressure. The constraining rings enable the FHPA to act like a shaftless multihinge structure with improved flexibility and more DOFs. It is noted that higher elasticity of the actuator backbone facilitates the bending of FHPA, while higher rigidity improves the stability and force output of the FHPA. Thus, in this design, a leaf spring is used as the elastic backbone of the FHPA. The transverse stiffness of the leaf spring is much larger than its axial stiffness, making it flexible in axial direction but stiff transversely. This leaf spring-based structure further improves the stability of the soft actuator and simplifies the deformation analysis of FHPA. As shown in Figure 1c, two end covers are utilized to fix the backbone and to seal the actuator. The bottom cover is connected with an air path tube

through a thread-through hole. Under actuation by air pressure, the FHPA bends along the leaf spring backbone through the expansion of the bladder chamber and the restricted layer on one side, mimicking the bending motion of human fingers. As shown in Figure 1b, the constraining rings are closely arranged with no gaps in between in the initial state; with the increase of the air pressure, the FHPA bends gradually and the constraining rings on the opposite side of the leaf spring are separated due to the extension of the central axis of actuator.

Figure 1d describes the assembly process of an FHPA. A rubber tube (Dalian Latex) is first trimmed to the desired length (Fig. 1d-i) and then sealed on its ends with two aluminum alloy plugs (Fig. 1d-ii). The bottom plug is screw threaded for the connection with the end cover. Then, a leaf spring (65Mn or Stainless steel) is fixed onto the end cover (Fig. 1d-iii) to control the bending direction of the FHPA. A set of constraining rings are then installed onto the rubber tube and leaf spring (Fig. 1d-iv). After that, the top-end cover is mounted onto the leaf spring and the threaded plug (Fig. 1d-v). The bottom-end cover is finally connected with a pneumatic connector (SMC) for pump actuation.

The proposed soft humanoid hand has demonstrated excellent adaptability and compatibility in grasping complex-shaped and fragile objects while simultaneously maintaining a high level of stiffness for exerting strong clamping forces to lift heavy loads (object weights up to 1.37 kg). This novel FHPA design enables the finger to deform easily but still maintains a large lateral stiffness for implementing complex tasks. The rigid components such as constraining rings and end covers are interfaced to the soft and elastic bladder to restrain its radial expansion without affecting its elongation or bending characteristics. As demonstrated in Figure 1e and Supplementary Video S2, the robotic hand is capable of grasping a variety of objects with different shapes, sizes, and weights (Supplementary Table S1). The two major postures, that is, enveloping and pinch grasping, can be easily achieved in grasping tasks. For the tip-pinch grasping, the thumb and the middle finger are actuated to press against each other to pick a Rubik's cube or a table tennis ball. For the enveloping grasping, the other four fingers can bend simultaneously and work together with the thumb finger to grasp a circular or cylindrical object with complex shapes.

Several assumptions are adopted to simplify the analysis of FHPAs: (1) the radial expansion of the inner rubber tube is fully constrained by the rings, the outer diameter of the pneumatic chamber remains unchanged when actuated by air pressure, and the bending profile of FHPA can be described as a circle shape (Fig. 2a); (2) the inner diameter of the chamber increases with its elongation and bending, while the wall thickness of chamber with the leaf spring remains nearly constant. To simplify the analysis, the wall thickness of chamber is assumed to be changed uniformly when air pressure is applied, and the circumference of inner wall of the bladder remains smooth. Therefore, the centerline of the chamber will offset a distance of e from its initial position after the bending deformation, as shown in Figure 2b; and (3) each constraining ring is fixed onto the leaf spring at the contact point like hinges, and they are independent and can rotate freely along the central lines when the FHPA bends. If ignoring the friction between the rubber tube and the constraining rings, the rings will only act to constrain the radial expansion of elastomer chamber and not generate any blocked moment for the bending of the FHPA.

As shown in Figure 2a, the cross section of the proposed FHPA is plane symmetrical. When an air pressure p is applied to the chamber, an axial force F_e is generated on the end cover, where $F_e = pS'$ and S' is the cross-sectional area of the bladder chamber, and it increases gradually due to the decrease of the wall thickness when FHPA bends. The resulting F_e produces a bending moment M_e, leading to the bending of the FHPA under the constraint of the leaf spring backbone. Without considering the thickness of the leaf spring, the bending neutral layer of FHPA coincides with the leaf spring because of the negligible length change of the leaf spring. Therefore, there are only two factors that affect the bending of the FHPA, the leaf spring and the rubber tube. We define M_s and M_r as the blocked bending moments generated by the leaf spring and the rubber tube, respectively. The bending radius of FHPA is defined as the distance between the bending center and the neutral layer, which can be expressed as $r = l_0/\theta$, where l_0 and θ are the original length and the bending angle of the FHPA, respectively. As a result, the elongation Δl of the central line of a FHPA can be calculated by $\Delta l = (H + e)\theta$, as shown in Figure 2b, where H is the distance from the center line of the chamber to the leaf spring in the initial state, e is the eccentricity due to the change of the chamber wall thickness when the FHPA bends.

Simple tension testing of a rubber tube is performed to check the stress–strain relationship in actuation. As shown in Supplementary Figure S2a, with the two ends of a FHPA fixed on a tensile testing machine, displacement-controlled tensile tests were performed at room temperature, with a loading speed of 1 mm/min and elongation up to 75%. The averaged values of three repeated tests were used for analysis. The stress–strain relations of the FHPA under different conditions (the shape of constraining rings, the gap and thickness of the rings, and different air pressures) are shown in Supplementary Figure S2b, indicating a strong linear relationship. Thus, to simplify the calculation, it is assumed that the deformation of FHPA chamber can be captured with a linear elastic model for strain <70%.

Figure 2c shows the geometry and dimensions of the inner wall of the chamber in the initial state and the bending state. The eccentricity e can be calculated as $e = \frac{(D_2 - D_2')}{2}$, where D_2 and D_2' is the inner diameter of chamber in its original state and the bending state, respectively. For the actuators with multiple air chambers, the actuation moment M_e can be expressed as

$$M_e = \sum_{i=1}^{4} F_e H_i = \sum_{i=1}^{4} p_i S_i' H_i \qquad i = 1,\ 2,\ 3,\ 4 \tag{1}$$

where H_i is the force arm of the moment M_e, i is the number of the chamber. When the FHPA is composed of i chambers (Fig. 6), the arm force H_i can be calculated as

$$\begin{cases} H_1 = H + e & i = 1 \\ H_1 = H_2 = H + e & i = 2 \\ H_1 = H_2 = H + e,\ H_3 = 2H + e & i = 3 \\ H_1 = H_2 = H + e,\ H_3 = H_4 = 3H + e & i = 4 \end{cases} \tag{2}$$

The rubber material for the bladder is assumed to be isotropic and incompressible, with a Poisson ratio of 0.4–0.5.

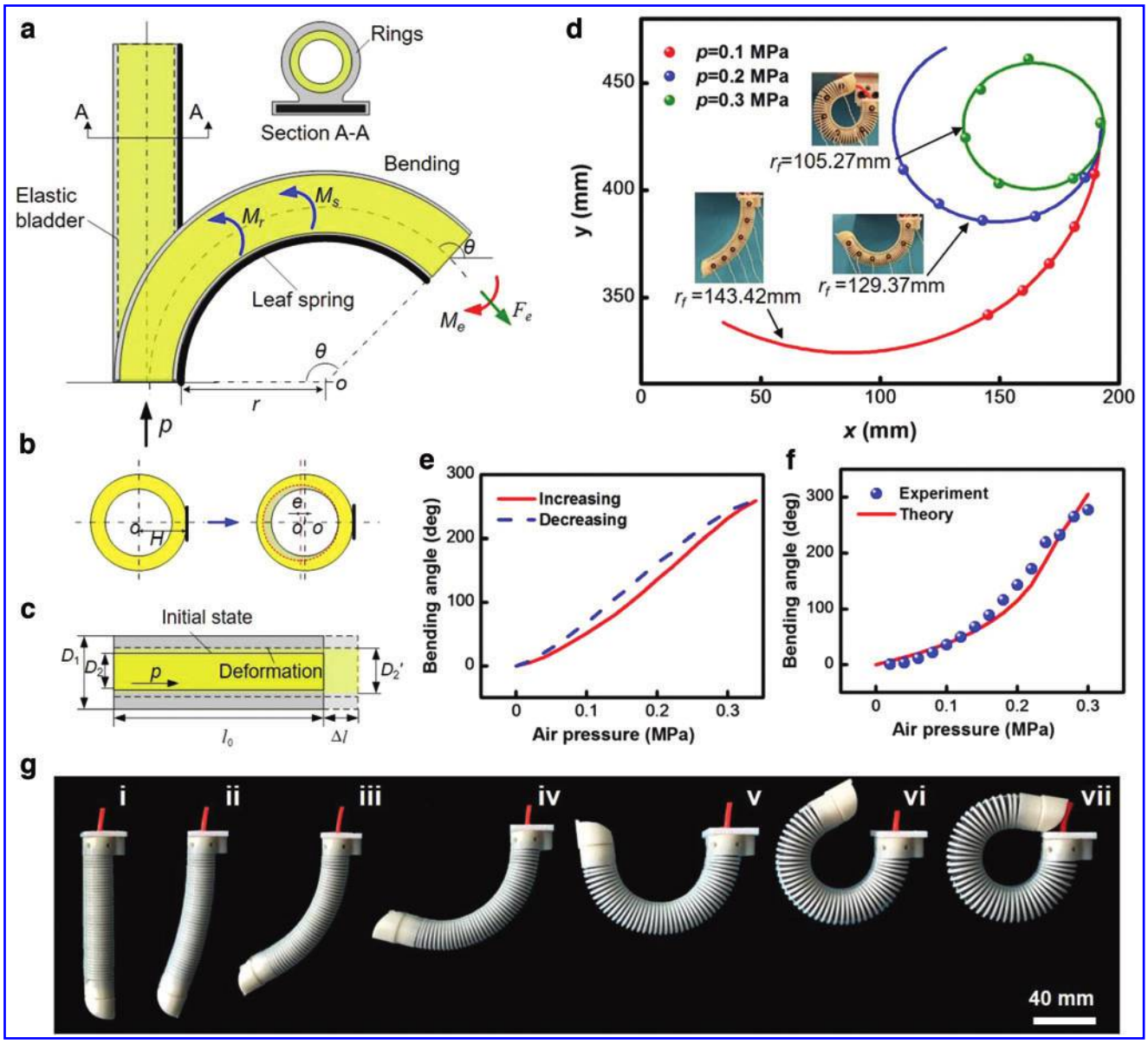

FIG. 2. Deformation analysis and actuation of a FHPA. **(a)** Geometry and deformation principle of a FHPA. **(b)** Cross section view and dimensions of the bladder, before and after deformation. **(c)** Side-view and dimensions of the artificial muscle before and after deformation. **(d)** Displacement and bending profiles under different air pressures, including both experimental data and fitted curves. **(e)** Variation of bending angles under inflation and deflation process. **(f)** Comparison of the bending angles between the theoretical and experimental data. **(g)** Photographs of the profile of the FHPA under different air pressures from 0 to 0.3 MPa. Color images are available online.

Thus, the volume of materials can be expressed as $V = \Delta S_0 l_0 = \Delta S'(l_0 + \Delta l)$, where ΔS_0 and $\Delta S'$ denote the annular cross-sectional area of the chamber in the initial and the bending state, respectively. As the FHPA bends, the gap between the constraining rings on the tension side will become larger and lead to the swelling of the rubber bladder along that side. Consequently, the correction ΔS is introduced to modify $\Delta S'$, and ΔS_0 and $\Delta S'$ can be expressed as

$$\begin{cases} \Delta S_0 = \frac{1}{4}\pi\left(D_1^2 - D_2^2\right) \\ \Delta S' = \frac{1}{4}\pi D_1^2 - S' + \Delta S \end{cases} \tag{3}$$

where D_1 is the outer diameter of the chamber; the modification ΔS is related to the shape, size, and gap of hoops, which can be obtained by comparing theoretical values with experimental data. Therefore, S' can be expressed as

$$S' = \frac{\pi(D_1^2 \Delta l + D_2^2 l_0)}{4(l_0 + \Delta l)} + \Delta S \tag{4}$$

Substituting Eqs. (2) and (4) into Eq. (1), one can obtain the momentM_e. Based on the assumption (3) and Euler–Bernoulli beam bending theory,[37] the resisting moments

generated by the leaf spring (M_s) and the bladder (M_r) can be expressed as

$$M_s = \frac{bE_1h^3}{12l_0(1-\mu^2)}\theta \tag{5}$$

$$M_r = \sum_{i=1}^{4} \frac{E_2I_2}{l_0/\theta + H_i} \tag{6}$$

where E_1, b, and h are the elastic modulus, width, and thickness of the leaf spring, respectively, μ is the Poisson ratio, E_2 is the elastic modulus of the elastic bladder, I_2 is the inertial moment of the chamber, and $I_2 = \frac{\pi(D_1^4 - D_2'^4)}{64} + \frac{\pi H_i^2(D_1^2 - D_2'^2)}{4}$. Thus, we can finally get $M_e = M_r + M_s$. This model can be used to predict the bending deformation of FHPA.

To verify the theoretical model for the bending deformation of FHPAs, experimental testing of 33 actuators with different parameters is performed to examine the influence of boundary conditions, dimensions, and number of chambers and materials. Figure 2d presents the deformation profiles of the FHPAs under an air pressure of 0.1, 0.2, and 0.3 MPa, respectively, in which the fitted lines from the experimental data show that the bending radius of the actuators reduces from 143.42 to 105.27 mm when the applied air pressure increases from 0.1 to 0.3 MPa. The radius error σ between bending deformation and fitting circle can be obtained by comparing distance d_i from the markers to the center of the fitting circle with the fitting radius r_f and calculated by $\sigma = \frac{\sum_{i=1}^{n}|d_i - r_f|}{nr_f} \times 100\%$. When the air pressure is 0.1, 0.2, and 0.3 MPa, the error σ between the experimental bending radius and the fitting circle is calculated to be 0.86%, 0.69%, and 0.35%, respectively. The larger initial error is due to the gap between the constraint rings and the rubber tube, and the actuator is not in full action at low air pressure. The error decreases with the increase of the air pressure (Fig. 2d). The maximum deviation of the bending angle of the actuator is 19.8% during inflation and deflation process (Fig. 2e), resulting from the hysteresis of the rubber.

In addition, because of the influence of the gravity of the actuator and the friction between the bladder and the constraining rings, the bending angles during deflation are slightly larger than those during the inflation process. As shown in Figure 2f and g, the actuators can bend up to a bending angle θ_{max} of 275° when an air pressure of 0.3 MPa is applied. The bending angle increases nonlinearly with the applied pressure, with a relatively slow increase at the initial stage and a rapid increase afterward when the air pressure reaches beyond 0.15 MPa. Remarkably, as shown in Figure 2f, the predicted values from theoretical model agree very well with the experimental data, especially in the initial stage of the actuation with lower air pressures. The slight deviation at higher pressures ($p > 0.15$ MPa) is attributed to the incomplete constraint of chamber with the increasing gap size between the external stiff slice constraints. The chamber separated by the stiff slice constraints will bulge outwards when the bending angle of FHPA becomes large at high air pressures, resulting in a nonlinear enhancement of the actuator. When the air pressure exceeds 0.24 MPa, the nonlinearity of FHPA deformation slows down, making the experimental data close to the theoretical curve, but lower than the theoretical value.

The actuation force of the soft actuator is important for the performance in achieving different tasks. In this study, we characterize these two kinds of output forces: blocked force and normal output force, to analyze the performance of FHPA. Supplementary Figure S2a and b shows the experimental setup for measuring the blocked force at different positions of actuators in the FHPA upon air pressures. Supplementary Figure S2c illustrates the blocked force as a function of measured position on the FHPA when the applied air pressure is 0.1, 0.2, and 0.3 MPa, respectively. It can be seen that the blocked force increases with the increase of air pressure. For a specific actuation pressure, the blocked force first increases to a maximum value and then decreases along its length, that is, the actuation force reaches the maximum blocked force at the position of about $L = 20$ mm. Supplementary Figure S2d illustrates the method to measure the normal output force of the actuator with a six-dimensional (6D) force sensor. Supplementary Figure S2e displays the specific experimental platform. The value of the normal output force is zero at the moment when the actuator just gets in touch with the force sensor, and then the value increases as the air pressure. In other words, the normal output force is the force output of the actuator after it achieves a certain bending deformation.

Supplementary Figure S2f shows the relationship between the normal output force and the air pressure. It indicates that with the increase of the initial bending angle of actuator, the maximum normal output force decreases gradually, and the normal output force increases linearly with the increasing air pressure. Therefore, the bending deformation and the clamping force can be easily controlled and programmed by the applied air pressure. Based on the as-fabricated prototype of FHPA (weight ~ 50 g), the output force of a soft finger for the humanoid hand can be as large as 15 N at the working air pressure of 0.3 MPa. Its working frequency can reach over 3 Hz, comparable with the actuation frequency of a human finger.

We further study the major design factors of the actuator for optimizing its mechanical performance, including the geometry size/dimension of the actuator, the material properties, the constrained boundary conditions, and the number of chambers that are discussed in detail. The bending angle and the output force of the actuator are utilized to evaluate the performances of FHPA. In this study, a series of different types of FHPAs (Supplementary Table S2) are fabricated to study the influence of cylindrical ring on the deformation and the output force of the FHPA. The bending angle of the actuator is measured by a gyro sensor (MPU-6050, InvenSense, Inc.) mounted on the tip of the actuator (Fig. 3a).

The key geometric parameters of the FHPA include the thickness of the constraining ring (t), the gap between the constraint rings (δ), the actuator length (l), the chamber size (D_1, D_2), and the leaf spring size (b and h), as shown in Figure 3b. The bending angles of 10 different types of FHPAs under different air pressures are tested: five with cylindrical rings ($l = 40$ mm, $D_1 = 12$ mm, $D_2 = 9$ mm, $b = 8$ mm, $h = 0.2$ mm) (Fig. 3c) and the other five with torus rings ($l = 40$ mm, $D_1 = 11$ mm, $D_2 = 8$ mm, $b = 8$ mm, $h = 0.2$ mm) (Fig. 3d). It is found that the effect of the thickness t of these two shaped rings on the bending angle is opposite. Thicker cylindrical rings result in a smaller bending angle, while thicker torus rings lead to a larger bending angle. With the same type of constraining rings (torus ring, $t = 2$ mm), rubber

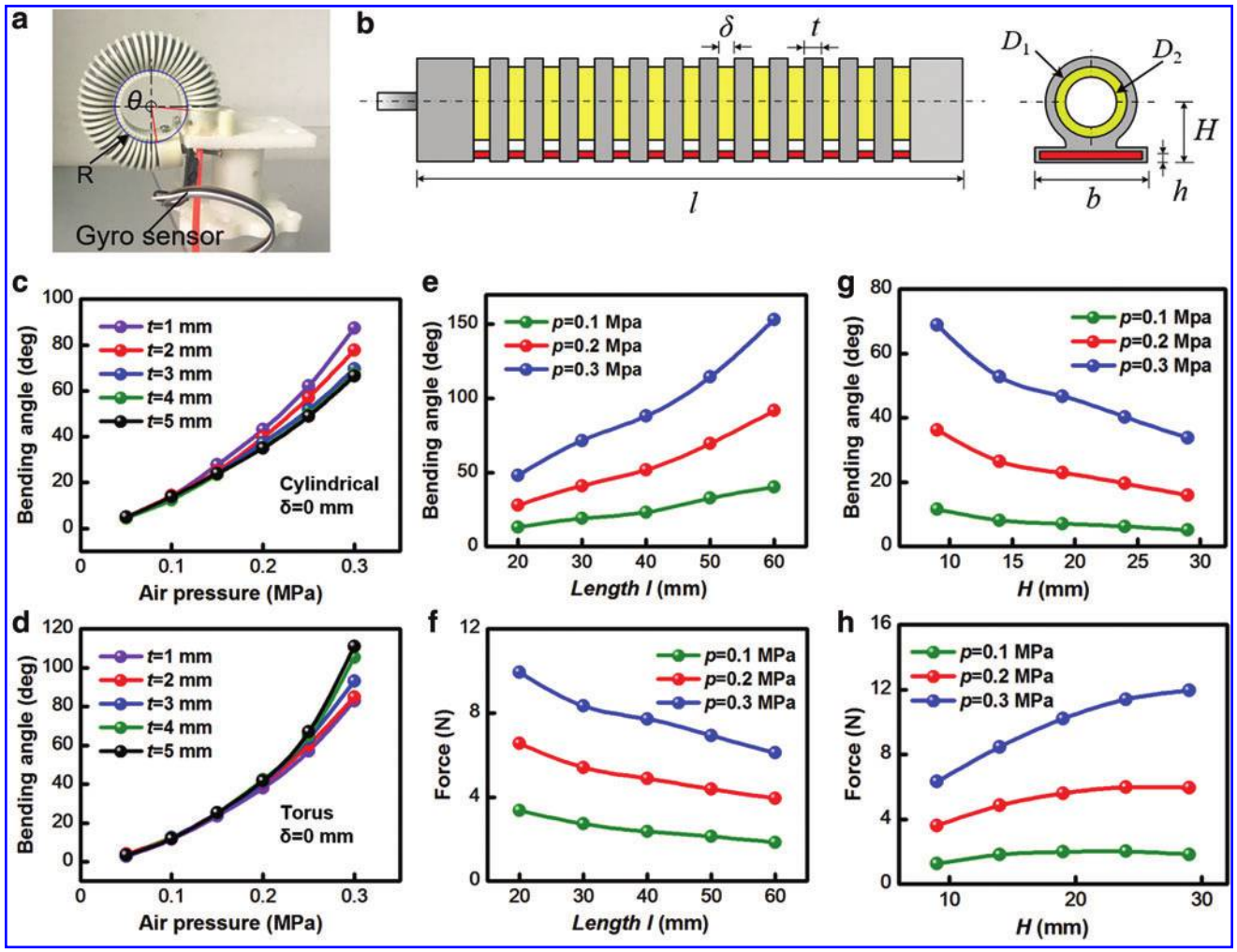

FIG. 3. Effect of the geometry of an FHPA on its performance. **(a)** The experimental setup for measuring the bending angle of the FHPA. **(b)** Schematic illustration of the geometric parameters of a single chamber FHPA. Variation of the bending angle of a FHPA with applied air pressure for different widths of the **(c)** cylindrical-shaped and **(d)** torus-shaped constraint ring. Variation of the **(e)** bending angle and **(f)** generated force of a FHPA as a function of body length l under different applied air pressures. Variation of the **(g)** bending angle and **(h)** generated force of a FHPA as a function of arm height H under different applied air pressures. Color images are available online.

tube (latex, $D_1 = 11$ mm, $D_2 = 8$ mm), and leaf spring (65Mn, $b = 8$ mm, $h = 0.25$ mm), five actuators with different lengths (l) ranging from 20 to 60 mm are tested to assess the influence of the FHPA length on its bending angle and normal force. It is observed that the bending angle increases with the applied air pressure and the increased length l, and every 10 mm increase of the actuator length leads to about 20° increase of the bending angle (Fig. 3e). However, the actuation force becomes smaller as the actuator length l increases (Fig. 3f).

In contrast, we test another five FHPAs having the same rubber tube (latex, $D_1 = 11$ mm, $D_2 = 8$ mm, $l = 40$ mm) and leaf spring (65Mn, $b = 8$ mm, $h = 0.25$ mm) but different force arm H (ranging from 9 to 29 mm) to examine the effect of H on its bending angle and normal force. It is obvious that the bending angle of FHPA decreases significantly with the increase of the force arm H (Fig. 3g), and the normal force only slightly increases with the force arm H (Fig. 3h). It is also noted that the force does not change significantly when the force arm is larger than 15 mm. The experimental results demonstrate that the FHPA has better performance when the force arm H is in the range of 8 ~ 14 mm when its length l is <60 mm.

In addition, the influences of the thickness and the width of the leaf spring on the performance of FHPAs are studied. For a fixed width $b = 12$ mm, the FHPA containing a thicker leaf spring generates a smaller bending angle but larger normal force (Fig. 4a, b). When the leaf spring thickness is fixed ($h = 0.25$ mm), FHPA bends less but generates larger force when it has a larger leaf spring width (Fig. 4c, d). This phenomenon actually agrees well with the theoretical analysis by Eq. (5), which also indicates that the increase of either thickness h or width b of leaf spring will result in a decreased bending angle of the FHPA. However, it should be noted that the influence of the geometry of the leaf spring on the normal force of the FHPA is limited and becomes negligible for larger values. It is also found that the elastic bladder with larger diameters ($D_1 = 15$ mm, $D_2 = 12$ mm) can generate slightly larger bending angle and significantly larger output force compared with the tubes with smaller diameters

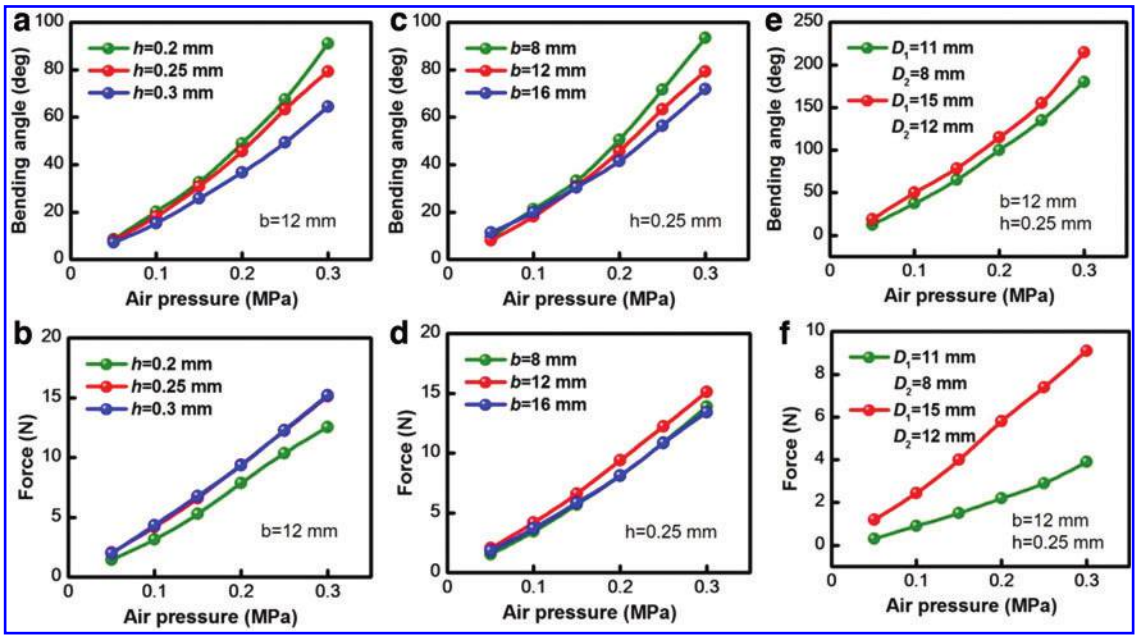

FIG. 4. Effects of leaf spring and bladder parameters on the bending performance of an FHPA. **(a, b)** The effects of width of leaf spring (b) on bending angle and output force. **(c, d)** The effects of thickness of leaf spring (h) on bending angle and output force. **(e, f)** The effects of outer diameter (D_1) and inner diameter (D_2) of chamber on bending angle and output force. Color images are available online.

($D_1 = 8$ mm, $D_2 = 11$ mm) (Fig. 4e, f), although it definitely needs a longer time to inflate a larger chamber to reach a specific pressure for actuation.

The proposed FHPA consists of both soft and rigid materials and, thus, combines the advantages of the deformability, adaptability, and compliance of the softness, while maintaining the large output force originated from the rigidity of the actuator. Supplementary Figure S3 shows the variation of the bending angle and the output force of FHPAs with the applied air pressure when different kinds of materials are used for the bladder (i.e., hyperelastic latex or silicone rubber) and the leaf spring (65Mn Spring steel and SUS301 Stainless steel). The silicone rubber has lower elastic modulus and will generate larger bending deformation than the latex rubber under the same conditions. However, the material of the leaf spring has little effect on the bending deformation, achieving approximately the same bending angles under the same pressure condition, as shown in Supplementary Figure S3a.

In addition, the silicone rubber is more antiaging and anticorrosion compared with latex, which are favorable for a variety of applications. It is found that the FHPA with silicone rubber tube and Spring steel (65Mn) backbone has much greater output force than the other two designs due to the higher elastic modulus of Spring steel (Supplementary Fig. S3b). Despite producing a larger output force, the leaf spring made of Spring steel (65Mn) has the drawbacks of being brittle and fragile. The experimental results show that FHPAs with the Spring steel (65Mn) leaf spring cannot survive the fatigue testing of high strength and large deformation ($\theta = 180°$, 1 Hz) for a long time. After cyclic bending for 26,400 times (Fig. 2g), the Spring steel (65Mn) leaf spring backbone breaks at the location of the sixth constraining ring (about 12 mm away from the top), although the FHPA can still maintain the initial undeformed profile, without deviation from the central line position. In contrast, the FHPA with stainless steel leaf spring breaks due to the elastic bladder explosion after 41,400 cyclic bending ($\theta = 180°$, 1 Hz), and the stainless-steel leaf spring is slightly deformed, about 5° away from its center line.

The deformation and the cross-section shape of the inner rubber tube of the FHPA are obtained from the computed tomography (CT) scanning image produced by a Caliper-Quantum FX High Resolution CT. As shown in Figure 5a, the thickness of the chamber wall changes uniformly as the actuator bends, while the bladder wall bonded with the leaf spring has almost no deformation. The walls of the chamber become thinner gradually with an increasing distance away from the leaf spring, reaching a minimum value on the tension side. The external and internal deformations of the chambers of the actuators constrained by rings of different shapes (torus and cylindrical) are also compared. Then, the thicknesses of chamber walls are measured from the CT images using the software Analyzer. Figure 5b shows that the wall thickness and the inflation profiles of the chamber vary with the shape of constraining rings and the gap and thickness of the rings. Compared with cylindrical constraint rings, the contact between torus rings and the chamber surface is a line and, thus, has much smaller contact area, leading to a smaller radial constraint area (Fig. 5b). The wall thickness t_w of the chamber with torus constraining rings is thinner than that with cylindrical rings (Fig. 5c).

As depicted in Figure 5d, for the actuator with cylindrical rings, a smaller thickness t of a constraining ring will lead to a larger gap between the rings, thus a thinner wall thickness t_w of the bladder chamber. In contrast, for a specific ring thickness, the wall thickness t_w of the chamber becomes thinner as the gap clearance between constraining rings reduces from $\delta = 2$ mm to $\delta = 1$ mm (Fig. 5e). Figure 5f and g shows the relationship between the cross-sectional area

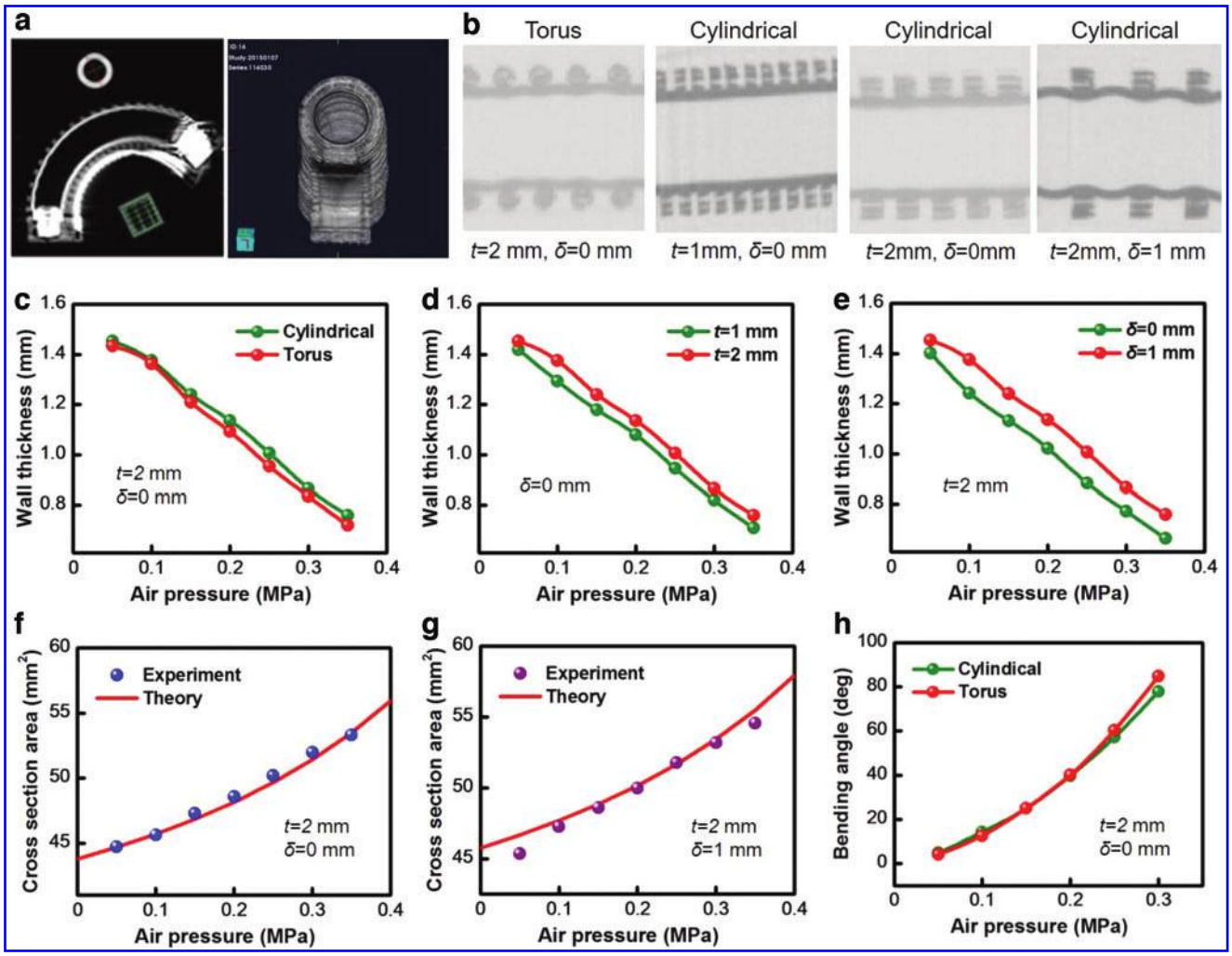

FIG. 5. Effect of constraint boundary on the working performance of an FHPA. **(a)** CT-image for the profile and deformation observation of FHPA chamber using a Caliper-Quantum FX High Resolution CT. **(b)** CT images of the contact deformations of the FHPA elastomeric bladders under different kinds of constraint boundaries. **(c)** Comparison of the constraint effect by different kinds of rings on the wall thickness of bladder for a fixed ring thickness $t = 2$ mm. **(d)** Variation of wall thickness of the FHPA bladder as a function of actuation pressure for different thicknesses of constraint rings $t = 1$, 2 mm. **(e)** Variation of wall thickness of the FHPA bladder as a function of actuation pressure for different gap clearances $\delta = 0$, 1 mm. **(f)** The change of cross-sectional area of the FHPA chamber with the applied actuation pressure for specific constraint rings without gap clearance. **(g)** The change of cross-sectional area of the FHPA chamber with the applied actuation pressure for specific constraint rings with a ring clearance of $\delta = 1$ mm. **(h)** The variation of the bending angles of a FHPA as a function of air pressure with different kinds of constraint rings. CT, computed tomography. Color images are available online.

(CSA) of the elastomeric bladder and the applied air pressure when the gap δ between constraining rings is equal to 0 and 1 mm, respectively. It can be seen that the theoretical results agree well with the experimental data. The increase of gap δ results in a reduced wall thickness and an increased CSA. The gaps between the constraining rings can enhance the flexibility and bendability of the hybrid actuator in actuation. Figure 5h shows the bending angles of the two kinds of FHPAs with cylindrical or torus constraining rings as a function of the applied air pressure. There is no obvious difference observed in the low-pressure working range; however, the bending angles of the FHPA with torus constraining rings are slightly larger than those with cylindrical rings in the high-pressure range.

We finally investigate the performance of FHPAs consisting of multiple chambers, including the configurations of single-chamber (S-C), dual-chamber (D-C), triple-chamber (T-C), and four-chamber (F-C) (Fig. 6a–d). As shown in Figure 6e, the bending angle and normal force of the FHPAs with different number of chambers are given as functions of the applied actuation pressure. It can be seen that the single-chamber FHPA produces the minimum bending angle, and the FHPA with two chambers generates the largest bending angle. However, there is no obvious difference between FHPAs with three or four chambers. The reason is that the increase of the number of chambers may affect both the active bending and resisting moments, leading to more complex variations. In contrast, it can be

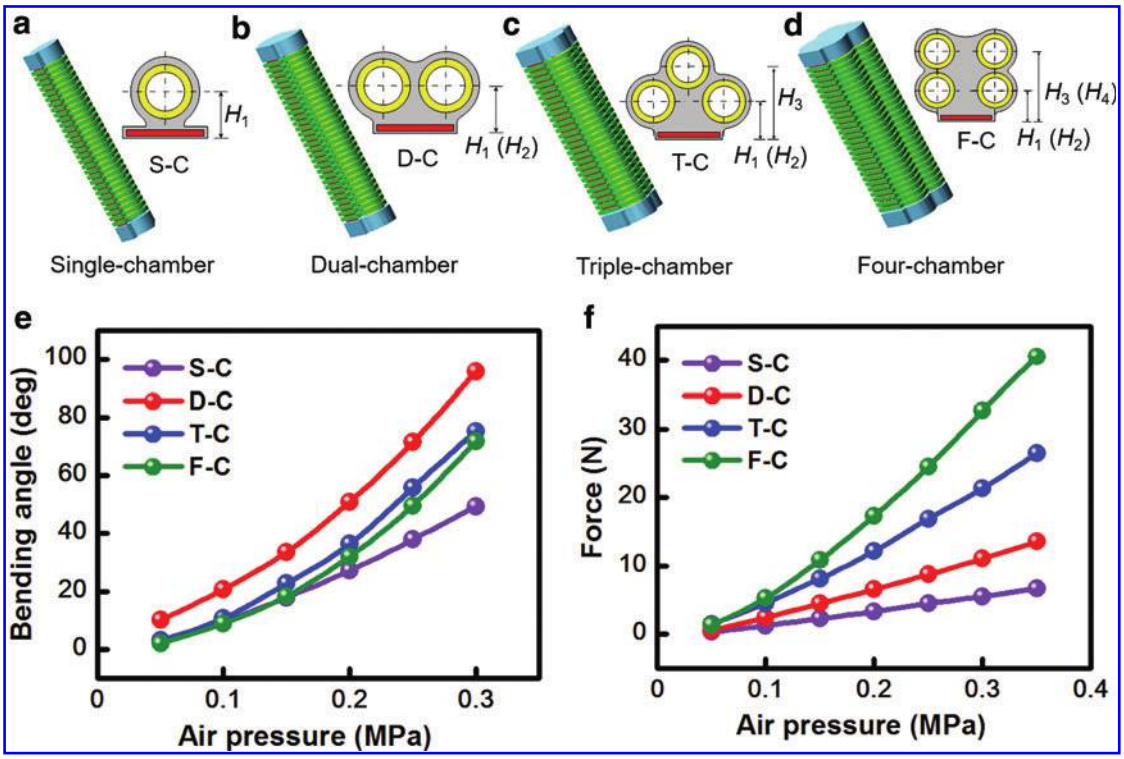

FIG. 6. Effect of chamber configuration on the performance of an FHPA. **(a–d)** Different configurations of the actuator body: single-chamber (S-C), Dual-chamber (D-C), Triple-chamber (T-C), and Four-chamber (F-C). **(e, f)** The effect of chamber configurations on the bending angles and actuation forces of the FHPA with the increasing applied pressure. Color images are available online.

observed that FHPAs with more chambers indeed generate larger actuation force. Experimental tests demonstrate that the maximum output force of a FHPA with four chambers can reach 42 N (Fig. 6f). Therefore, it will be desirable to use multiple chamber based FHPAs for implementing large grasping forces.

Conclusions

In summary, we have successfully developed a novel FHPA and a new design of the soft humanoid hand capable of grasping different kinds of objects robustly. The proposed theoretical model for the FHPA is verified by experimental investigations and valid for predicting the bending deformation and the grasping force under different conditions. The effects of the major design factors such as boundary condition, geometric, and material parameters on the overall performance of the actuator have been studied for further optimizing the soft robotic hand.

It is found that thicker cylindrical rings or torus rings thinner result in smaller bending angles, and for both types of constraining rings, the bending angle of FHPA increases with the applied air pressure, the increased length l, the reduced force arm H, and the increased thickness h or width b of leaf spring. The bending angles of the FHPA with torus constraining rings are slightly larger than those with cylindrical rings in the high-pressure range but no obvious difference observed in the low-pressure working range. The normal force of FHPA increases with the increasing force arm H, the decreasing length l, the wider leaf spring, and the number of chambers of the actuators.

This new soft humanoid hand exhibits the advantages of fast response, large grasping force, low cost, lightweight, and ease of fabrication and repair and is expected to be used in a variety of applications such as soft robotics, packaging automation, and agriculture harvesting.

Author Disclosure Statement

No competing financial interests exist.

Funding Information

X.L. and Y.Z. acknowledge the support from National Natural Science Foundation of China (51275004), Science and Technology Project of Department of Education of Jilin Province, China (JJKH20190640KJ). X.L. also thanks the support from China Scholarship Council (CSC201802325005). C.C. acknowledges the financial support from Michigan State University and the USDA National Institute of Food and Agriculture (Hatch project no. 1016788). X.T. acknowledges the support from MSU Strategic Partnership Grant (16-SPG-Full-3236).

Supplementary Material

Supplementary Table S1
Supplementary Table S2
Supplementary Figure S1
Supplementary Figure S2
Supplementary Figure S3
Supplementary Video S1
Supplementary Video S2

References

1. Kiang CT, Spowage A, Yoong CK. Review of control and sensor system of flexible manipulator. J Intell Robot Syst 2014;77:187–213.
2. Chen S, Pang Y, Yuan H, *et al*. Smart soft actuators and grippers enabled by self-powered tribo-skins. Adv Mater Technol 2020; DOI: 10.1002/admt.201901075.
3. Al Abeach LAT, Nefti-Meziani S, Davis S. Design of a variable stiffness soft dexterous gripper. Soft Robot 2017;4: 274–284.
4. Rus D, Tolley MT. Design, fabrication and control of soft robots. Nature 2015;521:8.
5. Sârbu F, Deaconescu A, Deaconescu T. Adjustable compliance soft gripper system. Int J Adv Robot Syst 2019;16: 1–10.
6. Tang Z, Lu J, Wang Z, *et al.* The development of a new variable stiffness soft gripper. Int J Adv Robot Syst 2019; 16; DOI: 10.1177/1729881419879824.
7. Park T, Kim K, Oh SR, *et al.* Electrohydraulic actuator for a soft gripper. Soft Robot 2020;7; DOI: 10.1089/soro.2019.0009.
8. Polygerinos P, Correll N, Morin SA, *et al.* Soft robotics: review of fluid-driven intrinsically soft devices; manufacturing, sensing, control, and applications in human-robot interaction. Adv Eng Mater 2017;19; DOI: 10.1002/adem.201700016.
9. Rodrigue H, Wang W, Kim D-R, *et al.* Curved shape memory alloy-based soft actuators and application to soft gripper. Compos Struct 2017;176:398–406.
10. Zhou X, Majidi C, O'Reilly OM. Soft hands: an analysis of some gripping mechanisms in soft robot design. Int J Solids Struct 2015;64–65:155–165.
11. Hughes J, Culha U, Giardina F, *et al.* Soft manipulators and grippers: a review. Front Robot AI 2016;3; DOI: 10.3389/frobt.2016.00069.
12. Shintake J, Cacucciolo V, Floreano D, *et al.* Soft robotic grippers. Adv Mater 2018;30:1707035.
13. Mosadegh B, Polygerinos P, Keplinger C, *et al.* Pneumatic networks for soft robotics that actuate rapidly. Adv Funct Mater 2014;24:2163–2170.
14. Deimel R, Brock, O. A novel type of compliant and underactuated robotic hand for dexterous grasping. Int J Robot Res 2015;35:161–185.
15. Al-Rubaiai M, Pinto T, Qian C, *et al.* Soft actuators with stiffness and shape modulation using 3d-printed conductive polylactic acid material. Soft Robot 2019;6:318–332.
16. Seok S, Onal CD, Cho K, *et al.* Meshworm: a peristaltic soft robot with antagonistic nickel titanium coil actuators. IEEE/ASME Trans Mechatron 2013;18:1485–1497.
17. Majidi C. Soft robotics: a perspective—current trends and prospects for the future. Soft Robot 2013;1:5–11.
18. Laschi C, Mazzolai B, Cianchetti M. Soft robotics: technologies and systems pushing the boundaries of robot abilities. Sci Robot 2016;1:eaah3690.
19. Petre I, Deaconescu A, Rogozea L, *et al.* Orthopaedic rehabilitation device actuated with pneumatic muscles. Int J Adv Robot Syst 2014;11:105.
20. Verma MS, Ainla A, Yang D, *et al.* A soft tube-climbing robot. Soft Robot 2018;5:133–137.
21. Yap HK, Ng HY, Yeow C-H. High-force soft printable pneumatics for soft robotic applications. Soft Robot 2016; 3:144–158.
22. Katzschmann RK, Marchese AD, Rus D. Hydraulic autonomous soft robotic fish for 3d swimming. Exp Robot 2016:405–420; DOI: 10.1007/978-3-319-23778-7_27.
23. Hassan T, Manti M, Passetti G, *et al.* Design and development of a bio-inspired, under-actuated soft gripper. In: Conference proceedings: Annual International Conference of the IEEE Engineering in Medicine and Biology Society. IEEE Engineering in Medicine and Biology Society. Annual Conference 2015;2015:3619.
24. Chen S, Cao Y, Sarparast M, *et al.* Soft crawling robots: design, actuation, and locomotion. Adv Mater Technol 2019; DOI: 10.1002/admt.201900837.
25. Wang W, Ahn, SH. Shape memory alloy-based soft gripper with variable stiffness for compliant and effective grasping. Soft Robot 2017;4:379–389.
26. Li J, Liu L, Liu Y, *et al.* Dielectric elastomer spring-roll bending actuators: applications in soft robotics and design. Soft Robot 2019;6:69–81.
27. Cao C, Zhao X. Tunable stiffness of electrorheological elastomers by designing mesostructures. Appl Phys Lett 2013;103:041901.
28. Tawk C, Gillett A, in het Panhuis M, *et al.* A 3d-printed omni-purpose soft gripper. IEEE Trans Robot 2019;35: 1268–1275.
29. Shapiro Y, Wolf A, Gabor K. Bi-bellows: pneumatic bending actuator. Sens Actuators A Phys 2011;167:484–494.
30. Giannaccini ME, Georgilas I, Horsfield I, *et al.* A variable compliance, soft gripper. Auton Robots 2014;36:93–107.
31. Galloway KC, Becker KP, Phillips B, *et al.* Soft robotic grippers for biological sampling on deep reefs. Soft Robot 2016;3:23–33.
32. Homberg BS, Katzschmann RK, Dogar MR, *et al.* Haptic identification of objects using a modular soft robotic gripper. In: 2015 IEEE/RSJ International Conference on Intelligent Robots and Systems (IROS), 2015.
33. Chen Y, Le S, Tan QC, *et al.* A reconfigurable hybrid actuator with rigid and soft components. In: 2017 IEEE International Conference on Robotics and Automation (ICRA), 2017.
34. Nemiroski A, Shevchenko YY, Stokes AA, *et al.* Arthrobots. Soft Robot 2017;4:183–190.
35. Fu, H-C, Ho, JDL, Lee K-H, *et al.* Interfacing soft and hard: a spring reinforced actuator. Soft Robot 2019;7:44–58.
36. Morton M. Rubber Technology. Netherlands: Springer Science & Business Media, 2013.
37. Wang, Q-M, Cross LE. Tip deflection and blocking force of soft pzt-based cantilever rainbow actuators. J Am Ceram Soc 1999;82:103–110.

Address correspondence to:
Changyong Cao
Laboratory for Soft Machines and Electronics
School of Packaging
Michigan State University
East Lansing, MI 48824
USA

E-mail: ccao@msu.edu

Yunwei Zhao
School of Mechanical Engineering
Beihua University
Jilin 132013
Jilin
China

E-mail: jluzyw@163.com